NASA Technical Memorandum 87212
SAE Paper No. 860615

A Two-Dimensional Numberical Study of the Flow Inside the Combustion Chamber of a Motored Rotary Engine

T.I-P. Shih and S.L. Yang
University of Florida
Gainesville, Florida

and

H.J. Schock
Lewis Research Center
Cleveland, Ohio

Prepared for the
1986 SAE International Congress and Exposition
Detroit, Michigan, February 24–28, 1986

NASA

The Engineering Resource For Advancing Mobility

400 COMMONWEALTH DRIVE WARRENDALE, PA 15096

SAE Technical Paper Series

860615

A Two-Dimensional Numerical Study of the Flow Inside the Combustion Chamber of a Motored Rotary Engine

T.I-P. Shih and S.L. Yang
University of Florida

and

H.J. Schock
NASA Lewis Research Center

1986 SAE International Congress and Exposition
Detroit, Michigan
February 24–28, 1986

All SAE papers are abstracted and indexed in the SAE Global Mobility Database

SAE GLOBAL MOBILITY DATABASE

ISSN 0148-7191

860615

A Two-Dimensional Numerical Study of the Flow Inside the Combustion Chamber of a Motored Rotary Engine

T.I-P. Shih and S.L. Yang
University of Florida

and

H.J. Schock
NASA Lewis Research Center

ABSTRACT

A numerical study was performed to investigate the unsteady, multidimensional flow inside the combustion chambers of an idealized, two-dimensional, rotary engine under motored conditions. The numerical study was based on the time-dependent, two-dimensional, density-weighted, ensemble-averaged conservation equations of mass, specie, momentum, and total energy valid for two-component ideal gas mixtures. The ensemble-averaged conservation equations were closed by a $K-\epsilon$ model of turbulence. This $K-\epsilon$ model of turbulence was modified to account for some of the effects of compressibility, streamline curvature, low-Reynolds number, and preferential stress dissipation. Numerical solutions to the conservation equations were obtained by the highly efficient implicit-factored method of Beam and Warming. The grid system needed to obtain solutions were generated by an algebraic grid generation technique based on transfinite interpolation. Results of the numerical study are presented in graphical form illustrating the flow patterns during intake, compression, gaseous fuel injection, expansion, and exhaust.

DIFFICULTIES WITH THE SUPPLY of aviation gasoline in several parts of the world have given rise to the need for more fuel-efficient and multifuel-capability general aviation aircraft engines (1-3).* One engine that is well suited for general aviation aircraft and can meet the requirements of higher fuel-efficiency and a greater tolerance to fuels with broader specifications is the stratified-charge rotary engine (3).

In order to design more fuel-efficient and more fuel-tolerant stratified-charge rotary engines, it is necessary to have a good understanding of the physics (fluid flow, heat transfer, and combustion) that take place inside the engines' combustion chambers. Relatively few investigators have studied the physics taking place inside rotary engines. Experimental research in rotary engines so far has been confined to studies on engine performance and emissions (4-10) and to high-speed photographic studies of combustion (11,12). Mathematical research in rotary engines has been broader in scope but has been limited to quasi-dimensional (13-22) and one-dimensional (23,25) analyses. To date, no studies have reported details of the unsteady, multidimensional flowfield inside rotary engine combustion chambers.

The unsteady, multidimensional flowfield inside a rotary engine combustion chambers is complex. Owing to this complexity, progress towards understanding the details of this flowfield can only be made in a piecemeal manner by focusing on specific problems. Furthermore, it is necessary to first study simplified rotary engines and later study increasingly more realistic rotary engines.

The objective of this study was to use a numerical method to investigate the flow patterns inside one of the combustion chambers of a simplified rotary engine under motored conditions. The simplified rotary engine studied here was two-dimensional (i.e., it was a rotary engine of infinite width) with "planar" gaseous fuel injection into the combustion chamber during the compression process. Also it was assumed that there was no leakage across the seals. The present study constitutes the first attempt at numerically studying the unsteady, multidimensional flow inside rotary engines. This study was conducted for a motored configuration in order to compare model results to experimental data which will soon be available.

*Numbers in parentheses designate references at end of paper.

0148-7191/86/0224-0615$02.50

In this report the simplified rotary engine studied is described in detail. Afterwards, formulation of the problem along with the essence of the numerical method of solution are presented. Finally, results for one numerical simulation are presented illustrating the flow patterns during intake, compression, gaseous fuel injection, expansion, and exhaust.

DESCRIPTION OF PROBLEM

A motored, two-dimensional rotary engine is shown in Fig. 1. It consists of a housing, an intake port, an exhaust port, a gaseous fuel injector, a rotor, three seals, three combustion chambers (the three regions bounded by the rotor, housing, and seals), and a shaft. The equations that describe the geometry of this rotary engine are given in Refs. 26 and 27 and summarized in Table I. The Cartesian coordinates X_1 and Y_1 describing the inner surface of the housing (denoted as surface 1 in Fig. 1) are given by Eqs. (1) and (2) (Table I). The Cartesian coordinates X_2 and Y_2 describing the outer surface of the rotor (denoted as surface 2, 3, and 4 in Fig. 1) are given by Eqs. (3) to (12) (Table I). The geometry of the rotor pockets is given by Eqs. (10) to (12). Here, it is noted that the parameter C representing the distance between the rotor apex and the housing is set at 0.004 m which is somewhat large. The value chosen is to facilitate the numerical method of solution. Since leakage was not considered, the value chosen for C should not seriously affect the flow patterns. The origin and orientation of the Cartesian coordinate system is shown in Fig. 2(a).

For this motored rotary engine, as the rotor rotates inside the housing, each of the three combustion chambers goes through five processes in the following order: intake, compression, gaseous fuel injection, expansion, and exhaust. Because of this symmetry, we only need to study the physics taking place inside one of the three combustion chambers. The combustion chamber chosen is the region bounded by surfaces 1, 2, 5, and 6 in Fig. 1.

As mentioned previously, leakage across the seals was not considered. If leakage across the seals was considered, we could still study the physics of the airflow taking place inside the rotary engine by only analyzing one combustion chamber.

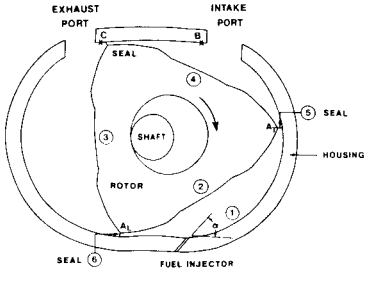

Figure 1. - Geometry of a two-dimensional rotary engine.

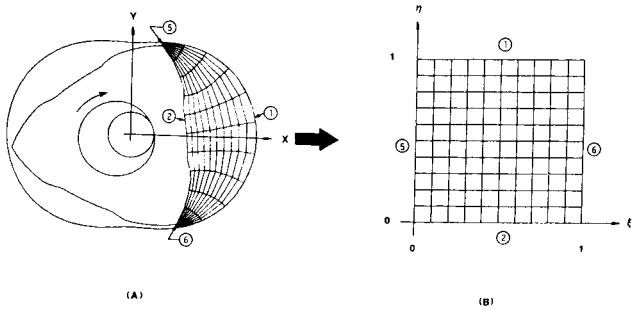

X-Y-t coordinate system. ξ-η-τ coordinate system

Figure 2. - Spatial domain the the coordinate system.

Initially, the combustion chamber to be studied is located at the beginning of the intake process (i.e., set θ in Eqs. (3) and (4) to zero) and is filled with stagnant air at a constant static temperature T_i and pressure P_i. Suddenly, the shaft starts to rotate at a constant angular velocity Ω of 5000 rpm (revolutions/min) which in turn causes the rotor to rotate in the clockwise direction. This starts the intake process.

During the intake process, air enters the combustion chamber through the intake port. The stagnation temperature T_o and pressure P_o ($P_o > P_i$, i.e., turbocharged) of the entering air are both constants. During the early part of the intake process, the exhaust port is also open. Thus some of the air also leaves the combustion chamber through the exhaust port. The back pressure of the exhaust port is maintained at P_{exh} ($P_{exh} < P_i$). Once the trailing apex (denoted by A_T in Fig. 1) passes point B on the housing (see Fig. 1), the intake port is closed. The reason for closing this port earlier is to facilitate the numerical method of solution. Once the intake port closes, the compression process starts. Later, between crank angles θ_1 and θ_2, a gaseous fuel (octane) is injected into the combustion chamber. Still later when the volume of the combustion chamber starts to increase, the expansion process starts. Once the leading apex (denoted by A_L in Fig. 1) passes point C on the housing (see Fig. 1), the exhaust port opens initiating the exhaust process. The late opening of the exhaust port is to facilitate the numerical method of solution. As noted earlier, the back pressure of the exhaust port is maintained constant.

For the problem just described, we are interested in knowing the details of the flow patterns inside the combustion chamber during intake, compression, gaseous fuel injection, expansion, and exhaust.

FORMULATION OF THE PROBLEM

The equations that govern the problem described in the previous section are the conservation equations of mass, species, momentum, and total energy for two-component ideal gas mixtures. In this numerical study, the following

TABLE I. - EQUATIONS DESCRIBING GEOMETRY OF ROTARY ENGINE[a]

Equation	Eq. No.
$X_1 = E \cos (3A) + (R + C) \cos (A)$	(1)
$Y_1 = E \sin (3A) + (R + C) \sin (A)$	(2)
$X_2 = E \sin (\theta) + X_{RO} \cos (\theta/3) + Y_{RO} \sin (\theta/3)$	(3)
$Y_2 = E \cos (\theta) + Y_{RO} \cos (\theta/3) - X_{RO} \sin (\theta/3)$	(4)
where	
$\theta = \int_0^t \Omega \, dt = \Omega t$	(5)
$X_{RO} = X_R \cos (\pi/6) + Y_R \sin (\pi/6)$	(6)
$Y_{RO} = Y_R \cos (\pi/6) + X_R \sin (\pi/6)$	(7)
$X_R = R \cos (2V) - (3E^2/R) \sin (6V) \sin (2V) + 2E \left[1 - (9E^2/R^2) \sin^2 (3V) \right]^{1/2} \cos (3V) \cos (2V) - P_x$	(8)
$Y_R = R \sin (2V) - (3E^2/R) \sin (6V) \cos (2V) + 2E \left[1 - (9E^2/R^2) \sin^2 (3V) \right]^{1/2} \cos (3V) \cos (2V) - P_y$	(9)
$P_x = P \cos (2V)$	(10)
$P_y = P \sin (2V)$	(11)
$P = \begin{cases} 0 & V_1 \le V \le V_T \\ \frac{P_1}{2} \left\{ 1 - \cos \left[\pi (V_1 - V)/(V_1 - V_2) \right] \right\} & V_2 \le V \le V_1 \\ P_2 + (P_1 - P_2)(V - V_3)/(V_2 - V_3) & V_3 \le V \le V_2 \\ \frac{P_2}{2} \left\{ 1 - \cos \left[\pi (V - V_4)/(V_3 - V_4) \right] \right\} & V_4 \le V \le V_3 \\ 0 & V_L \le V \le V_4 \end{cases}$	(12)

[a]A and V are parametric parameters. A varies between 0 and 2π. V varies between $V_L = \pi/6$ and $V_T = \pi/2$ for surface 2 (see Fig. 1); between $V_L = 5\pi/6$ and $V_T = 7\pi/6$ for surfaces 3; and between $V_L = 3\pi/2$ and $V_T = 11\pi/6$ for surface 4. E = 0.015 m, R = 0.1045 m, C = 0.004 m, $P_1 = P_2 = 0.005$ m, $V_1 = V_L + 0.75 (V_T - V_L)$, $V_2 = V_L + 0.625 (V_T - V_L)$, $V_3 = V_L = 0.375 (V_T - V_L)$, $V_4 = V_L + 0.25 (V_T - V_L)$, and $\Omega = 5000$ rpm.

simplifications were made to the conservation equations: (I) all thermodynamic and transport properties (except for the binary diffusion coefficient) were taken to be constants, (II) the binary diffusion coefficient was taken to be inversely proportional to the local mixture density, (III) pressure gradient contribution to specie diffusion and momentum transport due to species diffusion were neglected, (IV) irreversible coupling effects between the temperature gradient and the specie concentration gradient (Soret and Dufour effects) were neglected, (V) gravity force was not considered, (VI) bulk viscosity was taken to be zero, (VII)

radiation heat transfer was not considered, and (VIII) chemical reactions did not occur. Furthermore, since the flow of interest is turbulent and present computing capabilities prohibit direct or large eddy simulations of turbulence, the conservation equations were density-weighted, ensemble-averaged and closed by a K-ϵ model of turbulence (28). The K-ϵ model of turbulence employed was modified to account for some of the effects of compressibility (29), streamline curvature (30), low Reynolds number (31), and preferential stress dissipation (32).

The density-weighted, ensemble-averaged conservation equations and the K-ϵ model of turbulence used in this numerical study are summarized in Table II. Equations (13) to (44) in Table II constitute a closed system in seven dependent variables: density ($\overline{\rho}$), mass fraction of air ($\widetilde{X}_A$), x-component of the velocity ($\widetilde{u}$), y-component of the velocity ($\widetilde{v}$), total energy ($\widetilde{e}$), turbulent kinetic energy (K), and dissipation rate of turbulent kinetic energy (ϵ).

The boundary and initial conditions corresponding to Eqs. (13) to (44) are given in Table III. The no-slip condition requires the fluid velocity next to a solid wall to be equal to the velocity of the solid wall. This condition gives Eqs. (45) and (46). Here, it is noted that the K-ϵ model of turbulence employed was modified to account for some of the effects of low-Reynolds number so that the model can be applied all the way to the wall (i.e., wall functions are not needed).

The gas temperature next to a solid wall equals the temperature of the solid wall. With all walls maintained at given temperatures, this boundary condition results in Eqs. (47) and (48).

The walls are assumed to be nonporous. This boundary condition is expressed by Eq. (49).

The turbulent kinetic energy and the dissipation rate of turbulent kinetic energy are both set equal to zero at solid walls because of the turbulence model employed. These two boundary conditions are given by Eq. (50).

The stagnation temperature (T_o) and pressure (P_o) of the air entering the combustion chamber through the intake port are constant as reflected by Eqs. (51) and (52). The mass fraction of the air entering the combustion chamber through the intake port is unity and is given by Eq. (53). At the intake port, the x-component of the velocity is zero and the y-component of the velocity is determined by the Bernoulli equation. These two boundary conditions are given by Eqs. (54) and (55). The turbulent kinetic energy and the dissipation rate of turbulent kinetic energy of the air entering through the intake port are given by Eqs. (56) and (57).

At the fuel injector, gaseous fuel (octane) is injected into the combustion chamber when the crank angle θ is between θ_1 and θ_2. During fuel injection, the stagnation temperature of the fuel (T_f) is kept constant as shown by Eq. (58). The fuel is injected at an angle α into the combustion chamber (see Fig. 1). The xand y-components of the velocity are given by Eqs. (59) and (60). The first-derivative of the pressure normal to the fuel injector is taken to be zero. This boundary condition is given by Eq. (61). The turbulent kinetic energy and the dissipation rate of turbulent kinetic energy of the fuel at the fuel injector are given by Eqs. (62) and (63).

At the exhaust port, the back pressure (P_{exh}) is maintained constant. This condition is used to calculate the y-component of the velocity for the gas leaving the combustion chamber as indicated by Eq. (64). At the exhaust port, the x-component of the velocity along with the first-derivative with respect to y of the following variables are zero: mass fraction of air, pressure, temperature, turbulent kinetic energy, and dissipation rate of turbulent kinetic energy. These boundary conditions are given by Eqs. (65) and (66).

At time t equal to zero, the rotor is at the beginning of the intake process ($\theta = 0$) and the combustion chamber is filled with air at static pressure P_i and static temperature T_i. At this time, the air is in a state of homogeneous turbulence with zero mean velocity. The turbulent kinetic energy and the dissipation rate of turbulent kinetic energy of the air are both constant. These initial conditions are specified by Eqs. (67) to (72).

NUMERICAL METHOD OF SOLUTION

Solutions to the governing equations formulated in the above section can only be obtained by numercial methods. In this study, solutions were obtained by a finite-different method.

All finite-difference methods involve two approximations. First, the continuous domain of the problem must be replaced by time levels and a system of grid points. Second, the governing partial differential equations must be replaced by finite-difference equations. These two approximations are described below.

TIME LEVELS AND GRID SYSTEM - Finite-difference methods only provide solutions at the time levels and the grid points. The time increment between two successive time levels (i.e., the time-step size) must be made small enough to ensure numerical stability and temporal accuracy. For the present problem, the rotor is started impulsively from 0 to 5000 rpm. For such a problem, it is necessary to use a very small time-step size in the beginning (Courant number much smaller than unity). As time progresses, the time-step size used can be allowed to increase steadily until it reaches some preassigned value (corresponding to a Courant number much larger than unity). Such variable time-step sizes were employed here. The time-step size used between time levels n and n+1 (denoted by Δt^{n+1}) was as follows:

TABLE II. - GOVERNING EQUATIONS[a]

Equation	Eq. No.

$$\frac{\partial \bar{\rho}}{\partial t} + \frac{\partial}{\partial x}\bar{\rho}\tilde{u} + \frac{\partial}{\partial y}\bar{\rho}\tilde{v} = 0 \tag{13}$$

$$\frac{\partial}{\partial t}\bar{\rho}\tilde{X}_A + \frac{\partial}{\partial x}\bar{\rho u}\tilde{X}_A + \frac{\partial}{\partial y}\bar{\rho v}\tilde{X}_A = \frac{\partial}{\partial x} c_e \frac{\partial}{\partial x}\tilde{X}_A + \frac{\partial}{\partial y} c_e \frac{\partial}{\partial y}\tilde{X}_A \tag{14}$$

$$\frac{\partial}{\partial t}\bar{\rho}\tilde{u} + \frac{\partial}{\partial x}\bar{\rho}\tilde{u}^2 + \frac{\partial}{\partial y}\bar{\rho u v} = -\frac{\partial}{\partial x}\left(\bar{P} + \frac{2}{3}\bar{\rho}K\right) + \frac{\partial}{\partial x}\mu_e \tau^t_{xx} + \frac{\partial}{\partial y}\mu_e \tau^t_{yx} \tag{15}$$

$$\frac{\partial}{\partial t}\bar{\rho}\tilde{v} + \frac{\partial}{\partial x}\bar{\rho v u} + \frac{\partial}{\partial y}\bar{\rho}\tilde{v}^2 = -\frac{\partial}{\partial y}\left(\bar{P} + \frac{2}{3}\bar{\rho}K\right) + \frac{\partial}{\partial x}\mu_e \tau^t_{xy} + \frac{\partial}{\partial y}\mu_e \tau^t_{yy} \tag{16}$$

$$\begin{aligned}\frac{\partial \bar{e}}{\partial t} &+ \frac{\partial}{\partial x}\left(\bar{e} + \bar{P} + \frac{2}{3}\bar{\rho}K\right)\tilde{u} + \frac{\partial}{\partial y}\left(\bar{e} + \bar{P} + \frac{2}{3}\bar{\rho}K\right)\tilde{v} \\ &= \frac{\partial}{\partial x}\mu_e(\tau^t_{xx}\tilde{u} + \tau^t_{xy}\tilde{v}) + \frac{\partial}{\partial y}\mu_e(\tau^t_{yx}\tilde{u} + \tau^t_{yy}\tilde{v}) \\ &+ \frac{\partial}{\partial x}\lambda_e \frac{\partial \tilde{T}}{\partial x} + \frac{\partial}{\partial x}\left\{c_e\left[\left(h^o_A - h^o_B\right) + \left(C_{PA} - C_{PB}\right)\left(\tilde{T} - T_i\right)\right]\frac{\partial}{\partial x}\tilde{X}_A\right\} \\ &+ \frac{\partial}{\partial y}\lambda_e \frac{\partial \tilde{T}}{\partial y} + \frac{\partial}{\partial y}\left\{c_e\left[\left(h^o_A - h^o_B\right) + \left(C_{PA} - C_{PB}\right)\left(\tilde{T} - T_i\right)\right]\frac{\partial}{\partial y}\tilde{X}_A\right\}\end{aligned} \tag{17}$$

$$\frac{\partial}{\partial t}\bar{\rho}\tilde{K} + \frac{\partial}{\partial x}\bar{\rho u}\tilde{K} + \frac{\partial}{\partial y}\bar{\rho v}\tilde{K} = \frac{\partial}{\partial x}\left[\left(\mu + \frac{\mu_t}{\sigma_K}\right)\frac{\partial K}{\partial x}\right] + \frac{\partial}{\partial y}\left[\left(\mu + \frac{\mu_t}{\sigma_K}\right)\frac{\partial K}{\partial y}\right] + G - p\epsilon + D \tag{18}$$

$$\frac{\partial}{\partial t}\bar{\rho}\tilde{\epsilon} + \frac{\partial}{\partial x}\bar{\rho u}\tilde{\epsilon} + \frac{\partial}{\partial y}\bar{\rho v}\tilde{\epsilon} = \frac{\partial}{\partial x}\left[\left(\mu + \frac{\mu_t}{\sigma_t}\right)\frac{\partial \epsilon}{\partial x}\right] + \frac{\partial}{\partial y}\left[\left(\mu + \frac{\mu_t}{\sigma_\epsilon}\right)\frac{\partial \epsilon}{\partial y}\right] + S \tag{19}$$

where

$$\tau^t_{xx} = 2\frac{\partial \tilde{u}}{\partial x} - \frac{2}{3}\nabla \cdot \underset{\sim}{V} \tag{20}$$

$$\tau^t_{yy} = 2\frac{\partial \tilde{v}}{\partial y} - \frac{2}{3}\nabla \cdot \underset{\sim}{V} \tag{21}$$

$$\tau^t_{xy} = \tau^t_{yx} = \frac{\partial \tilde{u}}{\partial y} + \frac{\partial \tilde{v}}{\partial x} \tag{22}$$

$$\nabla \cdot \underset{\sim}{V} = \frac{\partial \tilde{u}}{\partial x} + \frac{\partial \tilde{v}}{\partial y} \tag{23}$$

$$\mu_e = \mu + \mu_t \tag{24}$$

$$\mu_t = C_\mu f_\mu \bar{\rho}K^2/\epsilon \tag{25}$$

$$c_e = \bar{\rho}D_{AB} + c_t \tag{26}$$

$$c_t = \mu_t/Sc_t \tag{27}$$

$$\lambda_e = \lambda + \lambda_t \tag{28}$$

TABLE II. - Continued.

$$\lambda_t = \mu_t C_p / Pr_t \tag{29}$$

$$\bar{P} = \left\{ \bar{e} - \bar{\rho}\tilde{X}_A \left[\left(h_A^o - h_B^o \right) - \left(C_{PA} - C_{PB} \right) T_i \right] - \bar{\rho} \left(h_B^o - C_{PB} T_i \right) - \frac{1}{2} \bar{\rho} \left(\tilde{u}^2 + \tilde{v}^2 \right) - \bar{\rho} K \right\} \left\{ R\bar{\rho}\tilde{X}_A \left(\frac{1}{M_A} - \frac{1}{M_B} \right) + \frac{R}{M_B} \bar{\rho} \right\} \Bigg/ \left\{ \left(C_{PA} - C_{PB} \right) \bar{\rho}\tilde{X}_A + C_{PB}\bar{\rho} \right] - \left[R\bar{\rho}\tilde{X}_A \left(\frac{1}{M_A} - \frac{1}{M_B} \right) + \frac{R}{M_B} \bar{\rho} \right] \right\} \tag{30}$$

$$\tilde{T} = \left\{ \bar{e} - \bar{\rho}\tilde{X}_A \left[\left(h_A^o - h_B^o \right) - \left(C_{PA} - C_{PB} \right) T_i \right] - \bar{\rho} \left(h_B^o - C_{PB} T_i \right) - \frac{1}{2} \bar{\rho} \left(\tilde{u}^2 + \tilde{v}^2 \right) - \bar{\rho} K \right\} \Bigg/ \left\{ \left[\left(C_{PA} - C_{PB} \right) \bar{\rho}\tilde{X}_a + C_{PB}\bar{\rho} \right] - \left[R \left(\frac{1}{M_A} - \frac{1}{M_B} \right) \bar{\rho}\tilde{X}_A + \frac{R}{M_B} \bar{\rho} \right] \right\} \tag{31}$$

$$G = \mu_t \left[2 \left(\frac{\partial \tilde{u}}{\partial x} \right)^2 + 2 \left(\frac{\partial \tilde{v}}{\partial y} \right)^2 + \left(\frac{\partial \tilde{v}}{\partial x} + \frac{\partial \tilde{u}}{\partial y} \right)^2 - \frac{2}{3} \nabla \cdot \underset{\sim}{V} \left(\mu_t \nabla \cdot \underset{\sim}{V} + \bar{\rho} K \right) \right] \tag{32}$$

$$S = C_1 f_1 \frac{\epsilon}{K} \left(C_1''' P_n + P_s \right) - C_2 f_2 \bar{\rho} \epsilon^2 / K + f_3 \tag{33}$$

$$P_n = \mu_t \left[2 \left(\frac{\partial \tilde{u}}{\partial x} \right)^2 + 2 \left(\frac{\partial \tilde{v}}{\partial y} \right)^2 \right] - \frac{2}{3} \mu_t C_1' (\nabla \cdot \underset{\sim}{V})^2 - \frac{2}{3} C_1'' \bar{\rho} K (\nabla \cdot \underset{\sim}{V}) \tag{34}$$

$$P_s = \mu_t \left(\frac{\partial \tilde{v}}{\partial x} + \frac{\partial \tilde{u}}{\partial y} \right)^2 \tag{35}$$

$$f_3 = \bar{\rho} \epsilon (\nabla \cdot \underset{\sim}{V}) + f_{BL} \left(\frac{2\mu\mu_t}{\bar{\rho}} \frac{\partial^2 \tilde{u}}{\partial \zeta^2} \right)^2 \tag{36}$$

$$C_1' = \left[C_1 + a \left(C_1 - 1.5 \right) \right] / C_1 \tag{37}$$

$$C_1'' = \left(3 + \frac{3}{2n} \right) / C_1 \tag{38}$$

$$a = 3 \left[\left(\frac{\partial \tilde{u}}{\partial x} \right)^2 + \left(\frac{\partial \tilde{v}}{\partial y} \right)^2 \right] \Bigg/ \left[\left| \frac{\partial \tilde{u}}{\partial x} \right| + \left| \frac{\partial \tilde{v}}{\partial y} \right| \right]^2 - 1 \tag{39}$$

$$n = 3 - \sqrt{2a} \tag{40}$$

$$D = f_{BL} \, 2\mu \left(\frac{\partial K^{1/2}}{\partial \zeta} \right)^2 \tag{41}$$

$$f_\mu = f_{BL} \exp \left[-3.4 \Big/ \left(1 + R_T/50 \right)^2 \right] + 1 \Big/ \left(1 + 0.57 \frac{K^2}{\epsilon^2} \frac{u_s}{r^2} \frac{\partial}{\partial r} r U_s \right) \tag{42}$$

$$f_2 = f_{BL} \left[1 - 0.3 \exp \left(- R_T^2 \right) \right] \tag{43}$$

$$R_T = \bar{\rho} K^2 \Big/ \mu\epsilon \tag{44}$$

TABLE II. - Concluded.

$^a\tilde{g}$ = density-weighted mean of g, $\tilde{g}$ = unweighted mean of g, $\bar{\rho}$ = density, $\tilde{u}$ = x-component velocity, $\tilde{v}$ = y-component velocity, $\bar{e}$ = total energy, $\bar{P}$ = pressure, $\tilde{T}$ = temperature, K = turbulent kinetic energy, ϵ = dissipation rate of turbulent kinetic energy, μ = dynamic viscosity, D_{AB} = binary diffusion coefficient, λ = thermal conductivity, C_{pi} = constant pressure specific heat of component i, M_i = molecular weight of component i, h_i^o = specific enthalpy of component i, T_i = reference temperature, R = universal gas constant, Sc_t = turbulent Schmidt number = 1, Pr_t = turbulent Prandtl number = 1, C_μ = 0.09, C_1 = 1.44, C_2 = 1.92, σ_K = 1.0, σ_ϵ = 1.3, $C_1'' = 2.24/C_1$, $\partial/\partial\zeta$ = derivative normal to the boundary, f_{BL} equals 1 in the boundary layer next to solid walls and equals 0 outside the boundary layer, f_1 = 1.0.

TABLE III. - BOUNDARY AND INITIAL CONDITIONS[a]

Location	Equation	Eq. No.
Housing surface	$\tilde{u} = \tilde{v} = o$	(45)
Rotor surface and apices	$\tilde{u} = \frac{\partial X_2}{\partial t}, \tilde{v} = \frac{\partial Y_2}{\partial t}$	(46)
Housing surface	$\tilde{T} = 300$ K	(47)
Rotor surface and apices	$\tilde{T} = 300$ K	(48)
Housing and rotor surfaces, apices	$\frac{\partial \tilde{X}_A}{\partial \zeta} = 0$	(49)
Housing and rotor surfaces, apices	$K = \epsilon = o$	(50)
Intake port	$P_o = 1.01 \times 10^5$ N/m^2	(51)
Intake port	$T_o = 300$ K	(52)
Intake port	$\tilde{X}_A = 1.0$	(53)
Intake port	$\tilde{u} = o$	(54)
Intake port	$\tilde{t} = - C_{DI} \left[2(P_o - \bar{P})/\bar{\rho} \right] 1/2$	(55)
Intake port	$K = \left(n_1 \tilde{v} \right)^2$	(56)
Intake port	$\epsilon = K^{3/2} \Big/ \left(n_2 L_1 \right)$	(57)
Fuel injector	$T_f = 300$ K	(58)
Fuel injector	$\tilde{v} = \left(V_o \sin \frac{\theta - \theta_1}{\theta_2 - \theta_1} \pi \right) \sin \alpha$	(59)

TABLE III. - Concluded.

Fuel injector	$\tilde{u} = \tilde{v}/\text{cotan}\ \alpha$	(60)
Fuel injector	$\frac{\partial \bar{P}}{\partial \zeta} = 0$	(61)
Fuel injector	$K = (n_3 \tilde{v})^2$	(62)
Fuel injector	$\epsilon = K^{3/2} \Big/ \left(n_4 L_2\right)$	(63)
Exhaust port	$\tilde{V} = C_{DE} \left[2\left(\bar{P} - P_{exh}\right) \Big/ \bar{\rho}\right]^{1/2}$	(64)
Exhaust port	$\tilde{u} = 0$	(65)
Exhaust port	$\frac{\partial}{\partial y} \tilde{X}_A = \frac{\partial}{\partial y} \bar{P} = \frac{\partial}{\partial y} \bar{T} = \frac{\partial}{\partial y} K = \frac{\partial}{\partial y} \epsilon = 0$	(66)
Everywhere inside the combustion chamber at $t = 0$	$\bar{\rho} = P_i \Big/ (RT_i/M_A)$	(67)
	$\tilde{X}_A = 1$	(68)
	$\tilde{u} = \tilde{v} = 0$	(69)
	$\bar{e} = P_i \left[\left(M_A C_{PA} - R\right) \Big/ R + \left(h_A^o - C_{PA} T_i\right)\right]$	(70)
	$K = \text{constant}$	(71)
	$\epsilon = \text{constant}$	(72)

$^a n_1 = 0.03$, $n_2 = 0.0075$, L_1 = intake port diameter, $V_o = 40$ m/sec, $n_3 = 0.03$, $n_4 = 0.0075$, L_2 = fuel injector diameter, C_{DI} = discharge coefficient for intake port, C_{DE} = discharge coefficient for the exhaust port, $P_i = 10^5$ N/m^2, $P_{exh} = 9.9 \times 10^4$ N/m^2.

$$\Delta t^{n+1} = \begin{cases} [\theta(n+1) - \theta(n)]/\Omega & n = 0,1,2,\ldots,n_s \\ \Delta\theta_f/\Omega & n = n_s + 1,\ n_s + 2,\ldots,n_t \end{cases} \tag{73}$$

where

$$\theta(n) = \theta_o + a_1 (n/n_s) + a_2 (n/n_s)^2 + a_3 (n/n_s)^3 \tag{74}$$

$$a_3 = \left[\Delta\theta_f + \Delta\theta_1 - 2(\theta_f - \theta_o)/n_s\right] \Big/ \left[1/n_s + 3/n_s^2 + 2/n_s^3\right] \tag{75}$$

$$a_2 = \left[\Delta\theta_1 - (\theta_f - \theta_o)/n_s - a_3 (1/n_s^3 - 1/n_s)\right] \Big/ \left[1/n_s^2 - 1/n_s\right] \tag{76}$$

$$a_1 = \theta_f - \theta_o - a_2 - a_3 \tag{77}$$

$$\Delta\theta_f = \left[6\pi - (\theta_f - \theta_o)\right] \Big/ \left[n_t - n_s\right] \tag{78}$$

In Eqs. (73) to (78), Ω is the angular speed of the shaft ($\Omega = 5000$ rpm). θ_o is the crank angle at which we begin computations ($\theta_o = 0$). θ_f is the crank angle after which the time-step size becomes a constant ($\theta_f = 1$ radian). The parameter n_s denotes the time level when $\theta = \theta_f$ ($n_s = 800$). $\Delta\theta_1$ is the crank angle traversed by the shaft during the first time step ($\Delta\theta_1 = 0.001\ \Delta\theta_f$). $\Delta\theta_f$ is the crank angle traversed by the shaft during each time step after time level $n = n_s$ or crank angle θ_f. The parameter n_t is the total number of time steps needed to traverse 6π crank angles ($n_t = 10\ 000$).

For computational efficiency, the number of grid points (intersections of grid lines) used should be kept to the minimum required to resolve spatially all significant features of

the flow. Here the system of grid points employed was as follows. In the x-y-t or Cartesian coordinate system (Fig. 2(a)), the grid points moved with the combustion chamber as the rotor rotated inside the housing. This reduced the number of grid points needed. To further reduce the number of grid points needed, grid points were clustered in regions where they are needed and widely spaced in regions where they are not needed. Here, more grid points were placed near the rotor, housing, and seals to resolve the steep gradients of the dependent variables in those regions. Finally, grid lines interesected the rotor and the housing perpendicularly to facilitate implementation of normal derivative boundary conditions.

To facilitate derivation of finite-difference equations, implementation of boundary conditions, and programming, the nonuniformly distributed and moving grid points in the x-y-t coordinate system were mapped onto another coordinate system, the ξ-η-τ coordinate system. In addition, grid lines in the x-y-t coordinate system corresponded to coordinate lines (i.e., lines of constant ξ or constant η) in the ξ-η-τ coordinate system.

This mapping of grid points is known as grid generation. Here, the mapping or grid generation was achieved by transfinite interpolation (33,34). The functional relationship between the two coordinate systems obtained by transfinite interpolation was derived in Ref. 34 and summarized by Eqs. (79) to (89) in Table IV.

FINITE-DIFFERENCE EQUATIONS - The finite difference equations used to approximate the governing equations summarized in Table II were derived by the implicit-factored method of Beam and Warming (35,36). The details of the finite-difference equations used along with their derivation were described elsewhere (37). Here, only the essence will be presented.

The first step in deriving the finite-difference equations was to replace all derivatives with respect to t, x, and y by derivatives with respect to τ, ξ, and η. The second step was to replace all derivatives with respect to τ (including the metric coefficients from the coordinate transformation) by the second-order accurate in time Crank-Nicolson time-difference formula. The third step was to employ a linearization procedure. The fourth step was to employ an approximate factorization procedure followed by splitting of the differential operator. Finally, all spatial derivatives (including the metric coefficients) were replaced by second order accurate in space central-difference formulas. Here it is noted that all metric coefficients were evaluated by finite difference formulas instead of by analytical differentiation. This was done to avoid geometrically induced errors (34,38).

The finite-difference equations derived by the steps described above formed systems of linear equations with block tridiagonal coefficient matrices and were solved by the noniterative Thomas' algorithm. These finite-difference equations provided the solutions at every grid point and time level presented in the next section.

RESULTS

Numerical solutions were generated to investigate the flow patterns inside the combustion chambers of the rotary engine depicted in Fig. 1 during intake, compression, gaseous fuel injection, expansion, and exhaust. Density, mass fractions of fuel and air, x- and y-components of the velocity, energy, temperature, pressure, turbulent kinetic energy, and dissipation rate of turbulent kinetic energy were calculated at 1071 (i.e., 51-by-21) grid points (see Fig. 3) for 10 000 time levels. Only results for the velocities (velocities relative to the stationary housing) are presented. These results are shown in Figs. 4 to 16 illustrating the flow patterns. Do not infer velocity gradients from these figures because the velocity vectors were plotted to best illustrate the flow patterns.

Figures 4 to 6 illustrate the flow patterns during the intake process. During the early part of the intake process, both the intake and the exhaust ports were open. Accordingly, air was found to enter the combustion chamber through the intake port and to exit through the exhaust port as shown in Fig. 4. Here, the stagnation pressure of the air entering the combustion chamber P_o was made slightly higher than the exhaust port back pressure P_{exh} (i.e., slightly turbocharged) so that back flow through the intake port did not occur. Later in the intake process, only the intake port was open and a high speed jet issued into

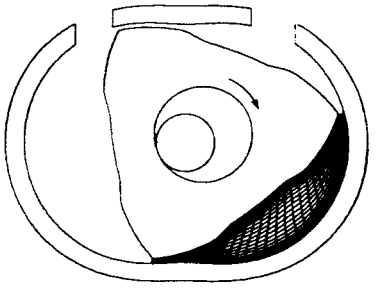

Figure 3. - Grid system.

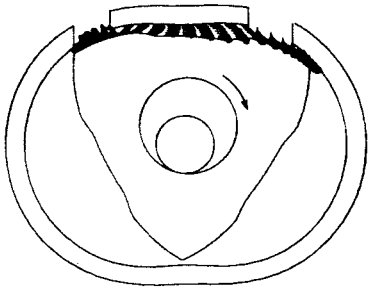

Figure 4. - Flow pattern at crank angle $\theta = .17$ radians or 10^{o}.

TABLE IV. - COORDINATE TRANSFORMATION[a]

Equation

$$X(\xi,\eta,\tau) = X_2(\xi,\tau)h_1(\eta') + X_1(\xi,\tau)h_2(\eta') - K_2(\xi)\frac{\partial Y_2(\xi,\tau)}{\partial \xi} h_3(\eta') - K_1(\xi)\frac{\partial Y_1(\xi,\tau)}{\partial \xi} h_4(\eta') \quad (79)$$

$$Y(\xi,\eta,\tau) = Y_2(\xi,\tau)h_1(\eta') + Y_1(\xi,\tau)h_2(\eta') + K_2(\xi)\frac{\partial X_2(\xi,\tau)}{\partial \xi} h_3(\eta') + K_1(\xi)\frac{\partial X_1(\xi,\tau)}{\partial \xi} h_4(\eta') \quad (80)$$

$$t = \tau \quad (81)$$

where

$$h_1(\eta') = 2(\eta')^3 - 3(\eta')^2 + 1 \quad (82)$$

$$h_2(\eta') = -2(\eta')^3 + 3(\eta')^2 \quad (83)$$

$$h_3(\eta') = (\eta')^3 - 2(\eta')^2 + \eta' \quad (84)$$

$$h_4(\eta') = (\eta')^3 - (\eta')^2 \quad (85)$$

$$\eta' = 0.5\left(B_\eta + 1\right) - B_\eta\left\{1 + \left[\left(B_\eta + 1\right)\Big/\left(B_\eta - 1\right)\right]^{(2\eta-1)}\right\}^{-1} \quad (86)$$

$$1 - \frac{A - A_L}{A_T - A_L} = 0.5\left(B_\xi + 1\right) - B_\xi\left\{1 + \left[\left(B_\xi + 1\right)\Big/\left(B_\xi - 1\right)\right]^{(2\xi-1)}\right\}^{-1} \quad (87)$$

$$1 - \frac{V - V_L}{V_T - V_L} = 0.5\left(B_\xi - 1\right) + B_\xi\left\{1 + \left[\left(B_\xi + 1\right)\Big/\left(B_\xi - 1\right)\right]^{(2\xi-1)}\right\}^{-1} \quad (88)$$

$$K_1(\xi) = K_2(\xi) = 2\left\{\left[X_1(\xi,\tau) - X_2(\xi,\tau)\right]^2 + \left[Y_1(\xi,\tau) - Y_2(\xi,\tau)\right]^2\right\}^{1/2} \quad (89)$$

[a] X_1, Y_1, X_2, and Y_2 are given by Eqs. (1) to (12) in Table I with the parameters A and V related to ξ as shown by Eqs. (87) and (88) in this table; $B_\xi = 0.1$; $B_\eta = 0.3$.

the combustion chamber (Figs. 5 and 6). In Fig. 6, a very small region of recirculating flow can be observed near the intake port. However, this recirculating flow region was found to appear aperiodically and then disappear. The disappearance of the recirculating flow is due to the general motion of the entire combustion chamber in one direction.

Figures 7 and 8 illustrate the flow patterns during compression. Recirculating flows were not observed during the compression process.

Figures 9 to 11 illustrate the flow patterns during gaseous fuel injection. Here gaseous fuel (octane) was injected into the combustion chamber between crank angles $\theta_1 = 7.4$ rad or 425° and $\theta_2 = 8.5$ rad or 487°. The velocity of the fuel jet was given by Eqs. (59) and (60) in Table III. The maximum speed of the fuel jet was $V_o = 60$ m/sec and the fuel was

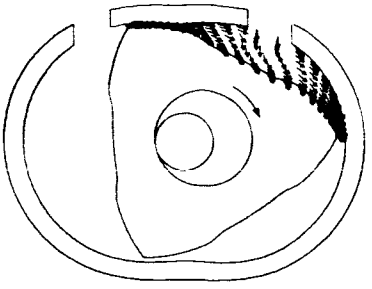

Figure 5. - Flow pattern at crank angle $\theta = 1.40$ radians or 80^{0}.

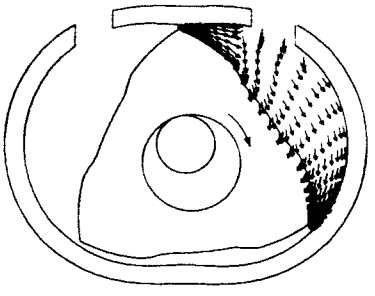

Figure 6. - Flow pattern at crack angle $\theta = 2.79$ radians or 160^{0}.

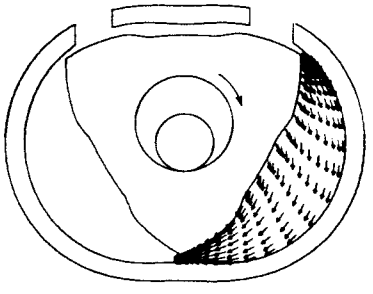

Figure 7. - Flow pattern at crank angle $\theta = 6.23$ radians or 357^{0}.

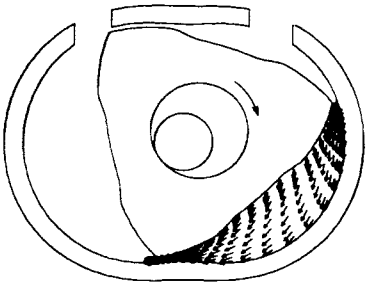

Figure 8. - Flow pattern at crank angle $\theta = 7.21$ radians or 413^{0}.

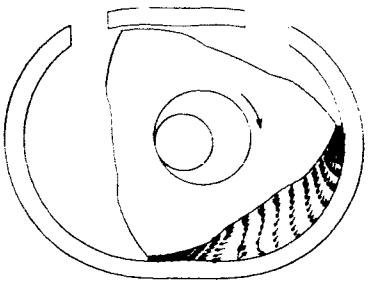

Figure 9. - Flow pattern at crank angle $\theta = 7.59$ radians or 435^{0}.

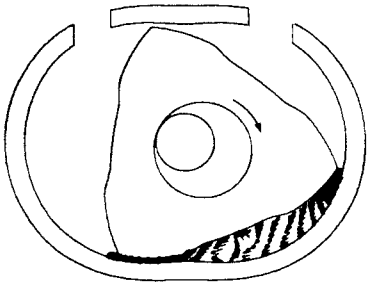

Figure 10. - Flow pattern at crank angle $\theta = 7.70$ radians or 441^{0}.

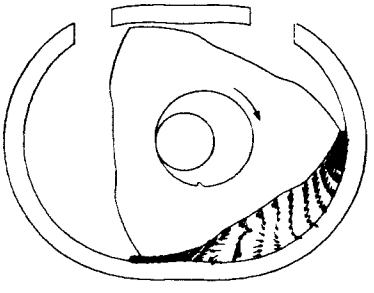

Figure 11. - Flow pattern at crank angle $\theta = 8.27$ radians or 474^{0}.

injected at an angle of $\alpha = 45°$ (see Fig. 1). When the fuel was first injected, its momentum was low in comparison to the momentum of the gas already inside the combustion chamber. Consequently, at this time the fuel jet could not penetrate very deeply into the combustion chamber as shown in Fig. 9. Later as the momentum of the fuel jet increased, it penetrated much deeper into the combustion chamber and a relatively large recirculating flow region can be observed as shown in Fig. 10. Towards the end of the fuel injection process, the momentum of the fuel jet was again low in comparison to the momentum of the gas inside the combustion chamber and the fuel jet was deflected as shown in Fig. 11.

SHIH

Results for the fuel injection process should be interpreted carefully. First, in realistic rotary engines, a liquid fuel instead of a gaseous fuel is injected. A liquid fuel jet has much more momentum than a gaseous fuel jet at identical jet velocities. Second and more important, in realistic rotary engines, the fuel jet invokes a three-dimensional phenomenon known as a jet in a crossflow. Jets in crossflows cannot be accounted for by two-dimensional numerical studies.

Figures 12 and 13 illustrate the flow patterns during the expansion process. No recirculating flow patterns were observed.

Figures 14 to 16 illustrate the flow patterns during exhaust. Here, we can observe some recirculating flows near the exhaust port as the gas rushed out of the combustion chamber.

The results presented above were not compared with other numerical or experimental data because they do not yet exist. As noted in the Introduction, the present study constitutes the first attempt at numercially studying the unsteady, multidimensional flow inside rotary engine combustion chambers.

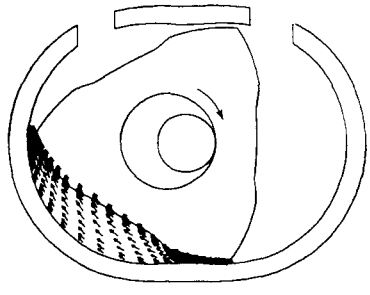

Figure 12. - Flow pattern at crank angle $\theta = 11.10$ radians or 436^{0}.

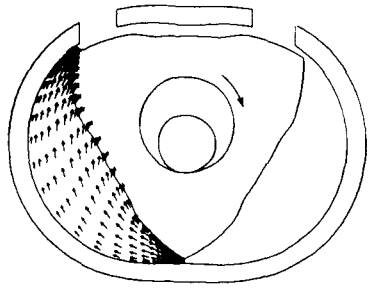

Figure 13. - Flow pattern at crank angle $\theta = 12.55$ radians or 719^{0}.

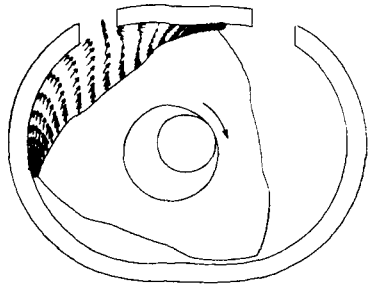

Figure 14. - Flow pattern at crank angle $\theta = 16.72$ radians or 958^{0}.

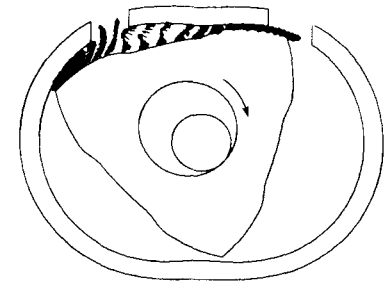

Figure 15. - Flow pattern at crank angle $\theta = 17.1$ radians or 980^{0}.

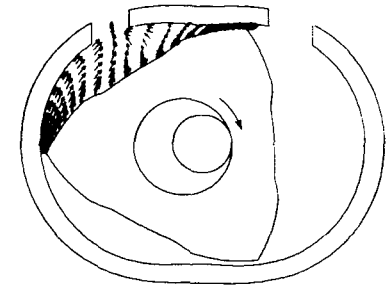

Figure 16. - Flow pattern at crank angle $\theta = 18.1$ radians or 1037^{0}.

CONCLUDING REMARKS

The results generated in this study illustrate some of the major features of the flow patterns taking place inside the combustion chambers of a two-dimensional rotary engine with gaseous fuel injection. From the results obtained so far, it appears that the mathematical model developed here can be used to study the effects of a number of engine design and operating parameters (such as those relating to the fuel injector, rotor pocket, engine speed, and intake-exhaust manifold pressure ratio) on the flow patterns.

Clearly, a two-dimensional study cannot account for all the important factors which influence combustion inside a real rotary engine. In particular, the effects of a jet in a crossflow (taking place during intake and fuel injection) as well as Taylor vortices can only be accounted for by a three-dimensional analysis. Since jets in crossflows and Taylor vortices can significantly affect the flowfield inside rotary engines, a three-dimensional numerical study is already underway.

REFERENCES

1. Willis, E.A., "General Aviation Internal-Combustion Engine Research Programs at NASA Lewis Research Center," NASA TM-78891, 1978.

2. Willis, E.A., and Strack, W.C., "An Overview of General Aviation Propulsion Research Programs at NASA Lewis Research Center," SAE paper No. 810624, 1981.

SHIH

3. Willis, E.A., "Development Potential of Intermittent Combustion (IC) Aircraft Engines for Commuter Transport Applications," SAE Paper No. 820718, 1982.

4. Jones, C., Lamping, H.D., Myer, D.M., and Loyd, R.W., "An Update of the Direct Injected Stratified Charge Rotary Combustion Engine Developments at Curtiss-Wright," SAE Paper No. 770044, 1977.

5. Jones, C. and Berkowitz, M., "Multifuel Rotary Aircraft Engine," AIAA Paper No. 80-1237, 1980.

6. Lamping, R.K., Manning, I., Meyer, D., and Tjoa, B., "Performance, Emissions, and Physical Characteristics of a Rotating Combustion Aircraft Engine," NASA CR-135119, Supplement A, 1980.

7. Schock, J.J., Rice, W.J., and Meng, P.R., "Experimental Analysis of IMEP in a Rotary Combustion Engine," SAE Paper No. 810150, 1981.

8. Meng, P.R., Rice, W.J., Schock, H.J., and Pringle, D.P., "Preliminary Results on Performance Testing of a Turbocharged Rotary Combustion Engine," SAE Paper No. 820354, 1982.

9. Cichanowize, J.E., and Sawyer, R.F., "Rotary Engine Combustion with Hydrogen Addition," SAE Paper No. 760611, 1976.

10. Burley, H.A., Meloney, M.R., and Stark, T.L., "Sources of Hydrocarbon Emissions in Rotary Engine," SAE Paper No. 780419, 1978.

11. Jones, C., "The Curtiss-Wright Rotary Combustion Engines Today," SAE Paper No. 886D, 1964.

12. Bayer, R.J., DeNagel, S.F., and Steiner, J.C., "Rotary Combustion Engine Hydrocarbon Source Studies," Paper presented at the Central States Section of the Combustion Institute, West Lafayette, Indiana, April 1978.

13. Eberle, M.K. and Klomp, E.D., "An Evaluation of the Potential Gain from Leakage Reduction in Rotary Engines," SAE Paper No. 730117, 1973.

14. Lawton, D., Miller, D.H., and Hutchinson, D.P., "Digital Simulation or Rotary Piston Engines," Paper C144/37, I Mech E Conference: Engine Performance Modeling, Institution of Mechanical Engineers, 1973.

15. Benson, R.S. and Sierens, R., "Some Gas Dynamic Studies in Wankel Engine," Paper 64/76, Proceedings of the Institution of Mechanical Engineers, 1976.

16. Benson, R.S. and Sierens, R., "Simulation of the Wave Action in the Inlet and Exhaust System and Calculation of the Burnt Mass Fraction in a Rotary Wankel Engine," Israel Journal of Technology, Vol. 15, 1977, pp. 209-221.

17. Blair, G.P. and Fleck, R., "The Unsteady Gas Flow Behavior in a Charge Cooled Rotary Piston Engine," SAE Paper No. 770763, 1977.

18. Danieli, G.A., Ferguson, C.R., Heywood, J.B., and Keck, J.C., "Predicting the Emissions and Performance Characteristics of a Wankel Engine," SAE Paper No. 740186, 1974.

19. Danieli, G.A., "A Performance Model of a Wankel Engine, Including the Effects of Burning Rates, Heat Transfer, Leakage and Quenching Compared with Measured Pressure Time Histories," Ph.D. Thesis, Dept. of Mechanical Engineering, MIT, 1976.

20. Danieli, G.A., Keck, J.C., and Heywood, J.B., "Experimental and Theoretical Analysis of Wankel Engine Performance," SAE Paper No. 780416, 1978.

21. Norman, T.J., "A Performance Model of a Spark Ignition Wankel Engine: Including the Effects of Crevice Volumes, Gas Leakage, and Heat Transfer," Master Thesis, Dept. of Mechanical Engineering, Massachusetts Institute of Technology, 1983.

22. Roberts, J.M., "Heat Release Estimation and Prediction of Wankel Stratified-Charge Combustion Engine," Master Thesis, Dept. of Mechanical Engineering, Massachusetts Institute of Technology, 1985.

23. Bracco, F.V. and Sirignano, W.A., "Theoretical Analysis of Wankel Engine Combustion," Combustion Science and Technology, Vol. 7, 1973, pp. 109-123.

24. Bracco, F.V. and Sirignano, W.A., "Theoretical Analysis of Stratified, Two-Phase Wankel Engine Combustion," Combustion Science and Technology, Vol. 8, 1973, pp. 69-84.

25. Reitz, R.D. and Bracco, F.V., "Studies Toward Optimal Charge Stratification in a Rotary Engine," Combustion Science and Technology, Vol. 12, 1976, pp. 63-74.

26. Ansdale, R.F., The Wankel RC Engine-Design and Performance, Iliffe Books Limited, London, 1968, pp. 131-139.

27. Yamamoto, K., Rotary Engine, Sankaido Co., Limited, Tokyo, Japan, 1981, pp. 11-13.

28. Shih, T.I-P., "Mathematical Models for the Numerical Study of Turbulent Flows," submitted to ASME J. of Fluids Engineering, 1985.

29. Morel, T. and Mansour, N.N., "Modeling of Turbulence in Internal Combustion Engines," SAE Paper No. 820040, 1982.

30. Leschziner, M.A. and Rodi, W., "Calculation of Annular and Twin Parallel Jets Using Various Discretization Schemes and Turbulence-Model Variations," ASME Journal of Fluids Engineering, Vol. 103, 1981, pp. 352-360.

31. Launder, B.E. and Sharma, B.I., "Application of the Energy-Dissipation Model of Turbulence to the Calculation of Flow Near a Spinning Disk," Letters in Heat and Mass Transfer, Vol. 1, 1974, pp. 131-138.

32. Hanjalic, K. and Launder, B.E., "Sensitizing the Dissipation Equation to Irrotational Strains," ASME Journal of Fluids Engineering, Vol. 102, 1980, pp. 456-461.

33. Smith, R.E., "Two-Boundary Grid Generation for the Solution of the Three Dimensional Compressible Navier-Stokes Equations," NASA TM-83123, 1981.

34. Yang, S.L. and Shih, T.I-P, "An Algebraic Grid Generation Technique for Time-Varying Two-Dimensional Spatial Domains," in press Int. J. for Numerical Methods in Fluids.

35. Beam, R.M. and Warming, R.F., "An Implicit Factored Scheme for the Compressible Navier-Stokes Equations," AIAA Journal, Vol. 16, 1978, pp. 393-402.

36. Shih, T.I-P., Smith, G.E., Springer, G.S., and Rimon, Y., "Boundary Conditions for the Solution of the Compressible Navier-Stokes Equations by an Implicit Factored Method," Journal of Computational Physics, Vol. 52, 1983, pp. 54-79.

37. Shih, T.I-P, Yang, S.L., and Schock, H.J., Jr., "Application of the Implicit-Factored Method to Two-Dimensional Unsteady Compressible Flow Problems with Arbitrary Geometries," to be submitted.

38. Hindman, R.G., "Generalized Coordinate Forms of Governing Fluid Equations and Associated Geometrically Induced Errors," AIAA Journal, Vol. 20, 1982, pp. 1359-1367.

1. Report No. NASA TM-87212 SAE Paper No. 860615	2. Government Accession No.	3. Recipient's Catalog No.

4. Title and Subtitle	5. Report Date
A Two-Dimensional Numerical Study of the Flow Inside the Combustion Chambers of a Motored Rotary Engine	6. Performing Organization Code 505-62-11
7. Author(s) T. I-P. Shih, S.L. Yang, and H.J. Schock	8. Performing Organization Report No. E-2871
	10. Work Unit No.
9. Performing Organization Name and Address National Aeronautics and Space Administration Lewis Research Center Cleveland, Ohio 44135	11. Contract or Grant No.
	13. Type of Report and Period Covered Technical Memorandum
12. Sponsoring Agency Name and Address National Aeronautics and Space Administration Washington, D.C. 20546	14. Sponsoring Agency Code

15. Supplementary Notes

Prepared for the 1986 SAE International Congress and Exposition, Detroit, Michigan, February 24-28, 1986. T. I-P. Shih and S.L. Yang, University of Florida, Gainesville, Florida 32611; H.J. Schock, NASA Lewis Research Center. This work was supported by NASA Grant NAG 3-363.

16. Abstract

A numerical study was performed to investigate the unsteady, multidimensional flow inside the combustion chambers of an idealized, two-dimensional, rotary engine under motored conditions. The numerical study was based on the time-dependent, two-dimensional, density-weighted, ensemble-averaged conservation equations of mass, specie, momentum, and total energy valid for two-component ideal gas mixtures. The ensemble-averaged conservation equations were closed by a $K-\epsilon$ model of turbulence. This $K-\epsilon$ model of turbulence was modified to account for some of the effects of compressibility, streamline curvature, low-Reynolds number, and preferential stress dissipation. Numerical solutions to the conservation equations were obtained by the highly efficient implicit-factored method of Beam and Warming. The grid system needed to obtain solutions were generated by an algebraic grid generation technique based on transfinite interpolation. Results of the numerical study are presented in graphical form illustrating the flow patterns during intake, compression, gaseous fuel injection, expansion, and exhaust.

17. Key Words (Suggested by Author(s))	18. Distribution Statement
Rotary engine; Flowfield; Two-dimensional simulation	Unclassified - unlimited STAR Category 02

19. Security Classif. (of this report)	20. Security Classif. (of this page)	21. No. of pages	22. Price*
Unclassified	Unclassified		

*For sale by the National Technical Information Service, Springfield, Virginia 22161